High Frequency Guided Wave Propagation and Scattering in Silicon Wafers

Jean-Luc Robyr [a)], Simon Mathieu [a), b)], Bernard Masserey [a)], and Paul Fromme [b)]

[a)] Department of Mechanical Engineering, HES-SO University of Applied Sciences and Arts Western Switzerland, Fribourg, Switzerland

[b)] Department of Mechanical Engineering, University College London, UK

Correspondence: p.fromme@ucl.ac.uk

Thin monocrystalline silicon wafers are employed for the manufacture of solar cells with high conversion efficiency. Micro-cracks can be induced by the wafer cutting process, leading to breakage of the fragile wafers. High frequency guided waves allow for the monitoring of wafers and detection and characterization of surface defects. The material anisotropy of the monocrystalline silicon leads to variations of the guided wave characteristics, depending on the guided wave mode and propagation direction relative to the crystal orientation. Selective excitation of the first anti-symmetric A_0 wave mode at 5 MHz center frequency was achieved experimentally using a custom-made wedge transducer. Strong wave pulses with limited beam skewing and widening were measured using non-contact laser interferometer measurements. This allowed the accurate characterization of the Lamb wave propagation and scattering at small artificial surface defects with a size of less than 100 µm. The surface extent of the defects of varying size was characterized using an optical microscope. The scattered guided wave field was evaluated, and characteristic parameters extracted and correlated to the defect size, allowing in principle detection of small defects. Further investigations are required to explain the systematic asymmetry of the guided wave field in the vicinity of the indents.

Keywords: Monocrystalline Silicon, Lamb Waves, Anisotropy, Ultrasonics, Surface Cracks

1. INTRODUCTION

Monocrystalline silicon wafers are used for the manufacture of solar photovoltaic panels with high conversion efficiency [1]. Thin wafers are beneficial to increase conversion efficiency and reduce manufacturing costs. However, in practice the minimum thickness of the brittle wafers is limited by wafer breakage rates due to surface micro-cracks induced by the wafer cutting process [2]. A range of nondestructive testing (NDT) techniques have been developed and proposed for the detection of micro-cracks in silicon wafers [3]. These include electroluminescence, thermography, optical transmission and interferometry imaging, impact testing, and ultrasonic wave propagation [4]. Resonance ultrasonic vibration techniques monitoring frequency shift and bandwidth of longitudinal vibration modes were proposed as indicators of millimeter sized cracks in silicon wafers [5].

Long propagation distances relative to the thickness of thin plate-like structures can be achieved employing guided ultrasonic waves [6]. For in-process monitoring this could provide the required full area coverage of silicon wafers during manufacture. The sensitivity of high frequency guided waves for crack detection in metallic plate structures has been demonstrated experimentally [7, 8], and mode conversion and nonlinear effects due to rough crack surfaces considered [9]. Guided wave scattering at horizontal cracks (disbonds) has been studied using modal expansion and Finite Element Analysis (FEA) [10]. The effects of anisotropy on guided wave propagation and defect detection have been widely investigated for composite structures, including the energy concentration along the fiber direction [11], modal focusing [12], and scattering at defects [13]. For an anisotropic multilayered structure, it has been demonstrated that a guided wave beam can deviate with respect to the sagittal plane of excitation towards the stiffer direction of the anisotropic structure [14]. For anisotropic silicon wafers the ultrasonic and guided wave propagation are direction dependent, but only limited experimental measurements have been reported. The variation of the arrival time and amplitude of the S_0

and SH modes with propagation direction was measured for silicon wafers and composite plates [15]. The focusing effect of silicon material anisotropy on the ultrasonic wave energy was predicted theoretically and measured experimentally [16, 17]. From an inversion of experimental data, the silicon material properties could be obtained [18]. The variation of zero group velocity, cut-off frequency, and amplitude with crystallographic orientation were measured using a line laser source [19]. The slowness surface of leaky Lamb waves for immersed silicon wafers was measured [20]. For monocrystalline silicon wafers, effects of the anisotropy on the propagation of the fundamental guided modes (A_0 and S_0) were measured and compared to Finite Element (FE) simulations and theoretical predictions [21]. Due to the anisotropy, significant guided wave skewing in the non-principal crystallographic directions was observed [22]. Especially for the S_0 mode, beam widening in directions away from the stiffest crystal orientation (<110>) and significant variation of the phase slowness occurs [21].

Laser interferometry measurements of the fundamental guided wave modes allowed crack detection in silicon wafers [23]. Using a B-scan configuration, the guided wave amplitude drop due to cracks in monocrystalline and polycrystalline silicon wafers was measured using air-coupled transducers [24]. For a circular measurement arrangement with air-coupled transducers, the amplitude profile of the A_0 mode at 200 kHz was recorded for different propagation directions [25]. This allowed the detection of a 20 mm long through-thickness notch in a wafer.

In this contribution, the scattering of the A_0 guided wave mode at 5 MHz center frequency was measured using a non-contact laser interferometer in the near field around small surface defects in thin monocrystalline silicon wafers. Using an indenter with different force levels, micro-defects of increasing severity were created and characterized using an optical microscope [26]. Section 2 provides details of the experimental measurements, including silicon wafer specimens and selective guided wave mode excitation and measurement. Section 3 provides a brief overview of guided wave propagation in the anisotropic, monocrystalline silicon wafers. Section 4 shows and compares the experimental results for the scattered wave field variation at defects of increasing severity, while section 5 concludes the paper.

2. EXPERIMENTS

2.1 Monocrystalline silicon specimens with artificial surface defects

Polished, boron doped P-type monocrystalline silicon wafers (001-cut) with a nominal thickness of 380 µm and 100 mm (4'') diameter were used in this study. An undamaged wafer was used to measure the guided wave excitation and propagation characteristics. In a second wafer, a cluster of 6 indents was made using a Vickers indenter at controlled speed and specified force. The indents were located on a predefined grid with a spacing of approximately 300 µm in both directions, with 2 indents per force level of 1 N, 1.5 N, and 2 N, respectively (Fig. 1b). Three additional silicon wafers were used for the investigation of the wave scattering at individual indents.

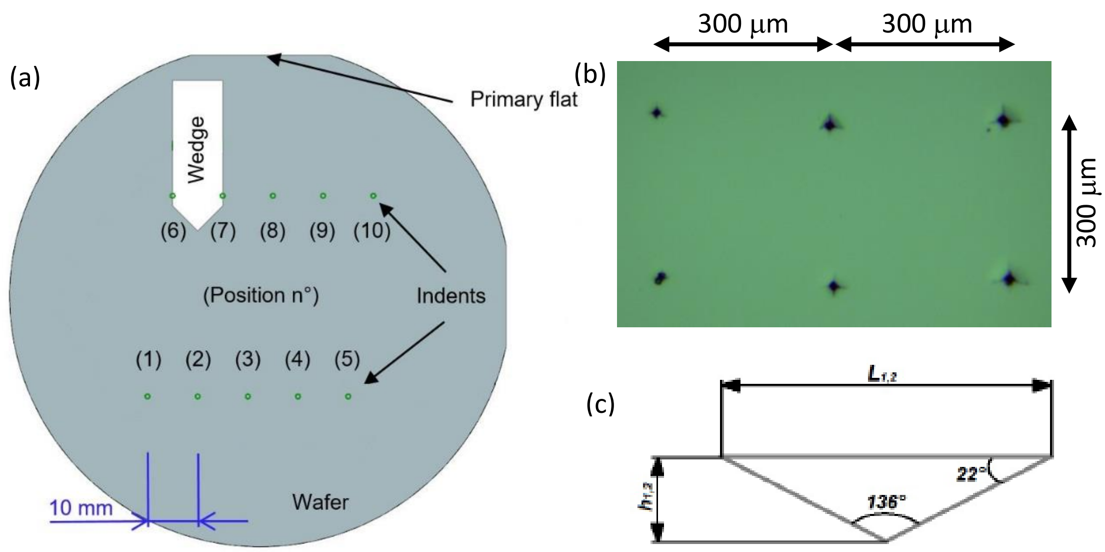

Figure 1: (a) Schematic of individual indent location and wedge position on wafer, 10 indents per wafer; (b) microscopy image of clustered pattern of 6 indents; (c) schematic of indenter geometry.

Each wafer contains 10 indents generated with the same force level (2 N, 3 N, and 4 N).The geometrical arrangement of the indents on a wafer is shown in Fig. 1a, with the indents placed in two lines with 10 mm separation between adjacent indents. All defects were made with a square (four-sided) pyramid indenter tip with an angle of 136° (Fig. 1c). The tip was oriented such that the four corners were along the highest stiffness directions <110>, which repeats every 90° for monocrystalline silicon.

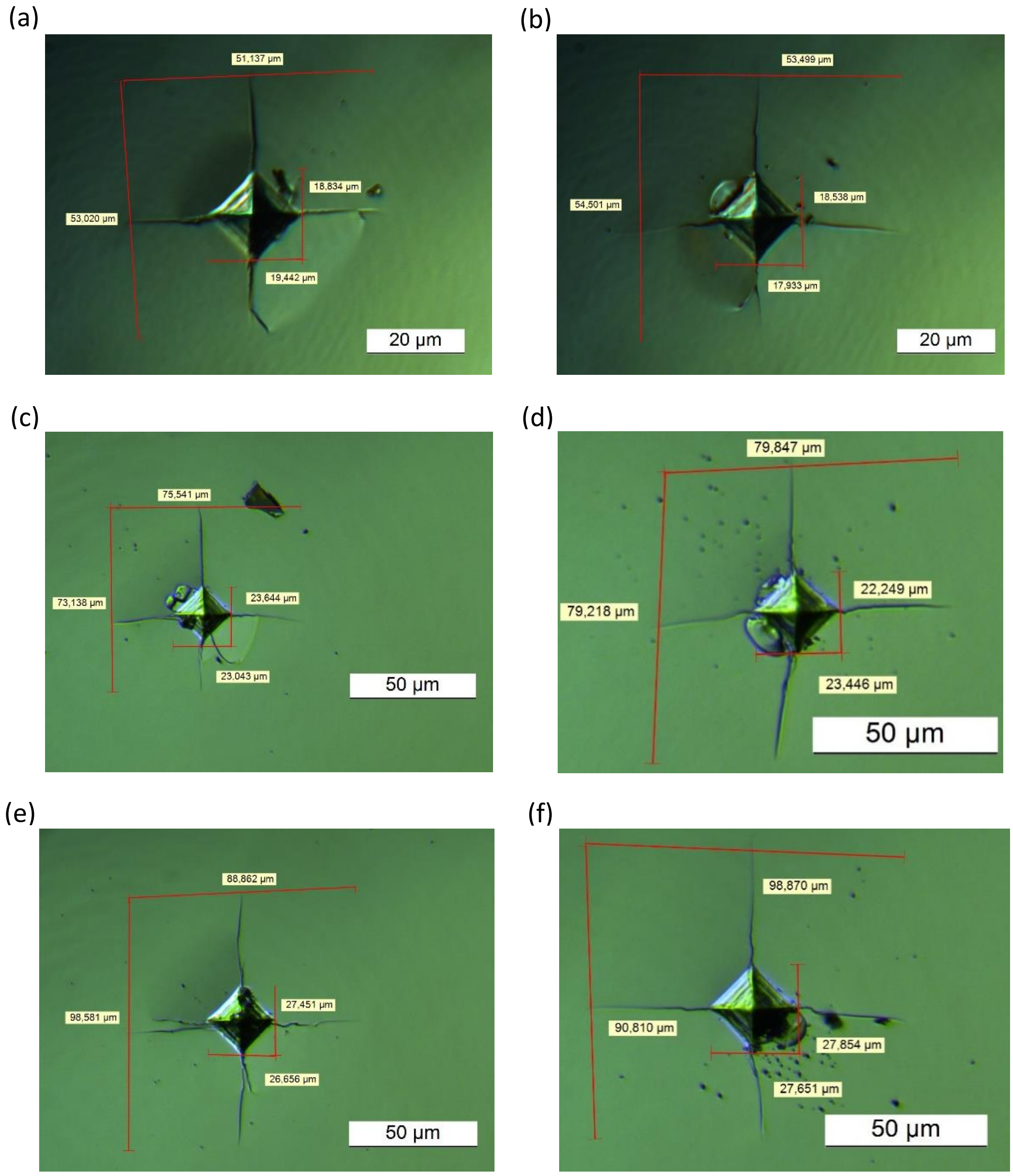

Figure 2: Microscopy photographs of individual defects with optical measurement of indent and overall defect size; (a), (b): 2N indent force; (c), (d): 3N indent force; (e), (f): 4N indent force.

From each of the corners a surface crack was generated along the highest stiffness directions <110> as shown in Fig. 2. Especially for the higher forces, chipping of the wafers adjacent to the indent was observed, and these defects were not investigated further. For each indenter force, at least two indents without visual indication of chipping at the surface were available. The surface extent of the indents and cracks was measured using an optical microscope, but no accurate depth information about the defects was available. The surface defect size showed a linear correlation with the indent force, with a maximum variation of the overall defect size of up to 10 µm for indents generated using the same force level (Fig. 3). From the measurement of the indent dimensions and the known angle of the indenter tip, the indent depth was estimated as 4 µm, 5 µm, and 6 µm for indent forces of 2 N, 3 N, and 4 N, respectively.

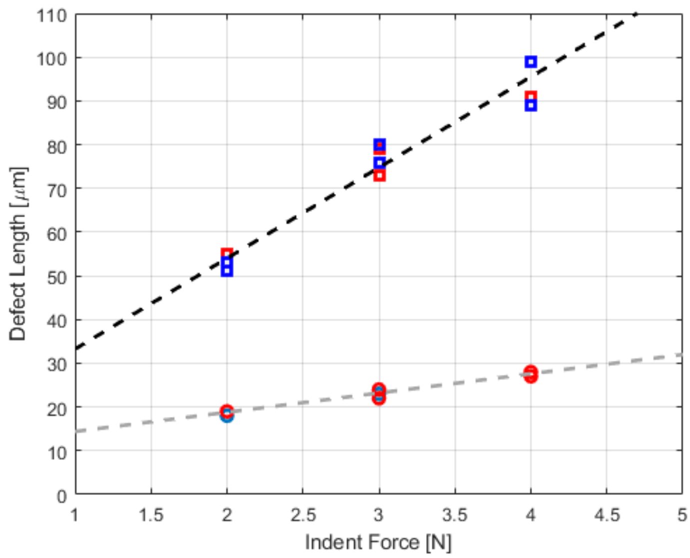

Figure 3: Optically measured defect size; square pyramid indent base (circles) and overall length including surface cracks (squares) against indent force (horizontal - blue; vertical - red); linear fit (dashed lines).

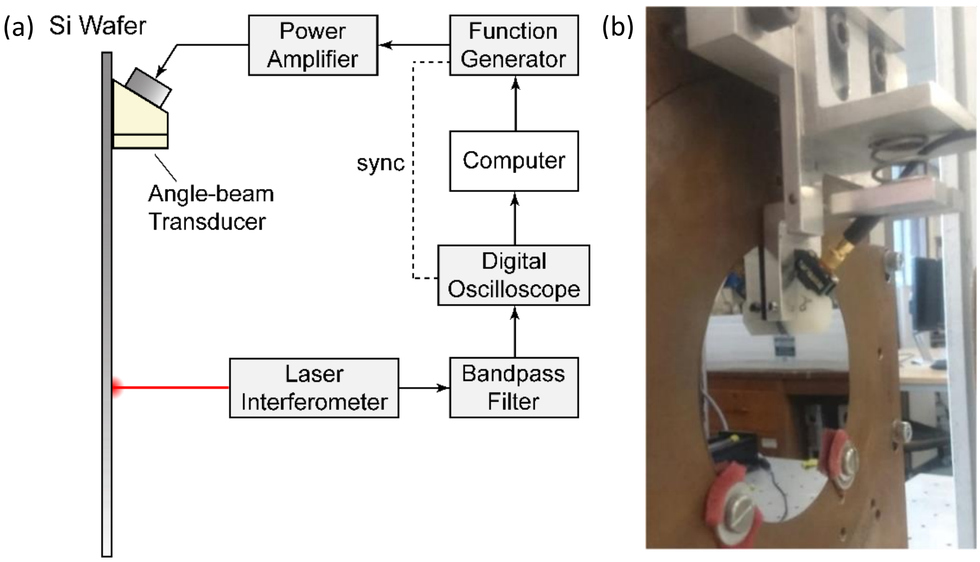

Figure 4: (a) Schematic diagram of the experimental setup; (b) photograph of monocrystalline silicon wafer on holder with spring-mounted wedge transducer.

2.2. Guided wave measurement

For the guided wave measurements, the silicon wafers were held in a custom-made wafer holder with a defined orientation against the flat (Fig. 4). This helped to reduce the risk of wafer breakage and allowed accurate angular orientation of the wafer with an accuracy of 1°. The A_0 guided wave mode (first anti-symmetric Lamb wave mode) was excited selectively at a center frequency of 5 MHz. A commercial piezoelectric transducer (width: 8 mm) was placed on a custom-made nylon wedge with an angle of 41° to match the wavelength for propagation along the <110> direction according to Snell's law and nominal phase velocity values. Using springs, the wedge was pressed against the silicon wafer with a controlled force of approximately 10 N [27]. Standard ultrasonic couplant was used on the contact surface and excess couplant removed before measurements. The excitation signal was defined in Labview as a narrowband Hanning-windowed sinusoidal pulse (12 cycles) with a center frequency of 5 MHz. The signal was generated using an arbitrary function generator and amplified to 400 V_{pp} using a power amplifier.

The out-of-plane surface displacement was measured using a non-contact, commercial laser interferometer. Very good laser beam reflection and signal to noise ratio (SNR) was obtained due to the mirror-like, polished silicon wafer surface, but care had to be taken to position the wafer exactly perpendicular to the laser beam. The laser head was moved parallel to the silicon wafer and holder using a positioning system with an accuracy and repeatability better than 1 µm. The measured out-of-plane displacement signal (output of laser demodulation) was bandpass filtered (2-8 MHz, 4^{th} order Butterworth filter) and recorded with a sampling frequency of 100 MHz using a digital storage oscilloscope. 40 averages at each measurement point were taken and the signal was transferred to a PC for evaluation in Matlab. The recorded time trace at each point was time-gated and the amplitude and phase values were extracted at the center frequency of 5 MHz using Fast Fourier Transform (FFT).

Initial measurements were conducted on the undamaged silicon wafer to characterize the guided wave field excited by the wedge transducer [18]. The chosen measurement grid had 9 steps of 5 mm in the wave propagation direction and 21 steps of 1 mm perpendicular to the wave propagation direction. Measurements were conducted for the wedge transducer aligned in both the <110> and <100> directions. For comparison, the field for the S_0 guided wave mode excited using the same setup, but with a custom-made wedge with an angle of 19° according to Snell’s law are shown [21]. For the silicon wafer with the clustered defect, the guided wave field over an area of 1000 µm by 600 µm, containing the 6 indents, was measured with a step size of 20 µm in horizontal and vertical directions. For the 3 silicon wafers containing individual defects, the scattered guided wave field was measured around two of the defects with the same indenter force and with no evidence of chipping. In order to accurately capture local amplitude variation close to each indent, an area of 400 µm by 400 µm was scanned with a step size of 5 µm in the horizontal and vertical direction. For the guided wave measurements, the exact defect location relative to the laser beam positioning could not be verified independently, and several steps were required to center the small measurement area approximately around the defect location [27, 28].

3. GUIDED WAVE PROPAGATION IN SILICON WAFERS

For the nominal silicon material properties (cubic symmetric stiffness constants: C_{11} = 165.70 GPa, C_{12} = 63.90 GPa, C_{44} =79.56 GPa, density ρ = 2390 kg/m^3) the guided wave propagation characteristics were predicted using the Disperse software [29]. The phase velocity of the fundamental S_0 mode shows a variation of approximately 10% between the propagation in the direction of highest stiffness <110> and lowest stiffness <100>. For the flexural A_0 mode a lower variation of approximately 3% was predicted. Good agreement with experimental measurements of the phase slowness was found in a previous publication [21]. The chosen excitation frequency of 5 MHz for a wafer thickness of 380 µm is marked in the dispersion diagram (Fig. 5). Good separation between the phase velocities of the fundamental A_0 and S_0 modes can be observed and both modes show reasonably low dispersion for the chosen frequency thickness product of approximately 2 MHz mm.

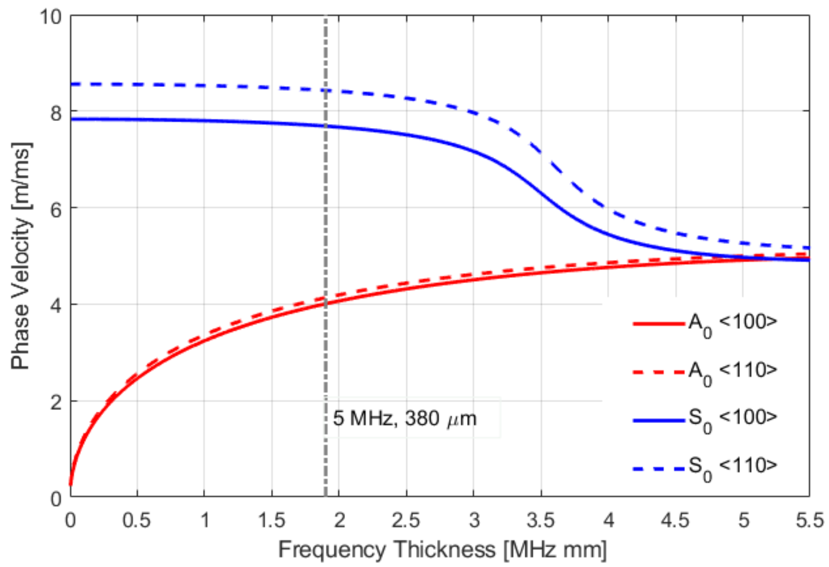

Figure 5: Dispersion diagram for silicon wafer, product of nominal thickness and excitation frequency marked.

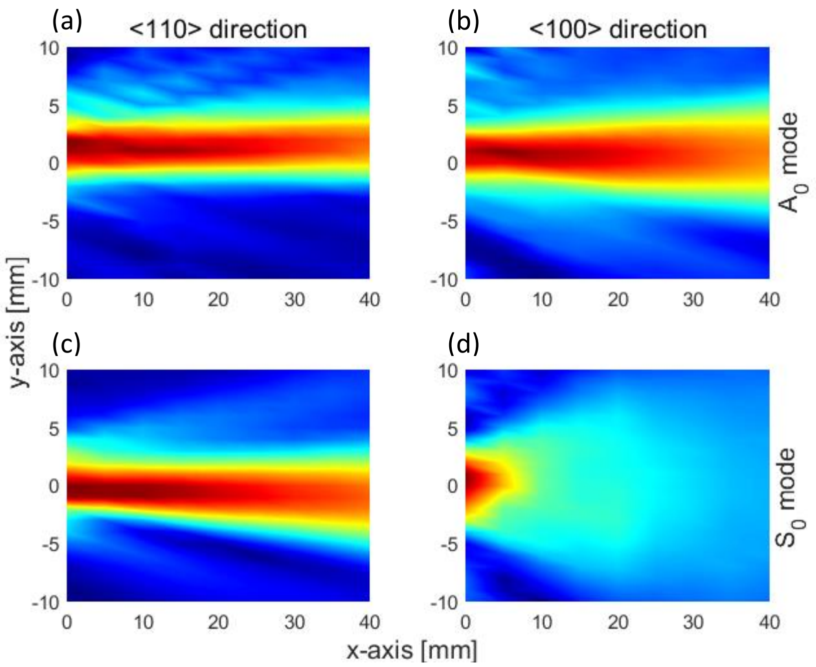

Figure 6: Measured guided wave field amplitude in front of the wedge transducer; (a) A_0 mode <110> direction; (b) A_0 mode <100> direction; (c) S_0 mode <110> direction; (d) S_0 mode <100> direction.

The guided wave propagation in front of the wedge transducer was characterized from the non-contact laser measurements. For the A_0 mode a strong wave beam with high amplitude was observed for the two principal directions (Fig. 6a/b), with some slight beam widening for the lower stiffness <100> direction (Fig. 6b). For the S_0 mode a strong wave beam was measured in the stiffer <110> principal direction (Fig. 6c), but significant beam widening in the lower stiffness <100> direction was observed, which significantly reduces the range for defect detection. Together with the significant wave skew angle of the S_0 mode in the non-principal directions due to the variation of the phase slowness [21] and a two times larger wavelength for the selected center frequency, the S_0 mode has some disadvantages for the monitoring of defects compared to the A_0 mode.

4. DEFECT SCATTERING

A first measurement of the guided wave interaction with a cluster of defects was conducted for the silicon wafer containing 6 indents with a spacing of approximately 300 µm (Fig. 7). The measurement was conducted with a step size of 20 µm in both directions to cover the area containing the defects. The amplitude of the guided wave field was normalized and corrected for the gradient of the incident wave by fitting and subtracting a plane with a linear gradient in the y-direction (propagation direction). The wave field shows some variability of up to 10% of the amplitude of the incident wave, which might likely be caused by changes in the coupling of the wedge transducer over the several hours of measurement duration. At the approximate location of each of the clustered defects, a clear amplitude peak can be observed. The maximum peak amplitude (normalized with the amplitude of the incident wave) increases in general with the severity of the defect, from approximately 1.2 for the 1 N defects to approximately 1.8 for the 2 N defects. Interestingly, for the 1.5 N defects, a variability in amplitude was observed, with normalized amplitudes of 1.3 and 1.9. Around each defect a roughly quarter-circular area of higher and lower amplitude similar to interference fringes was observed, but not of significantly higher amplitude than the variability of the measured guided wave field amplitude.

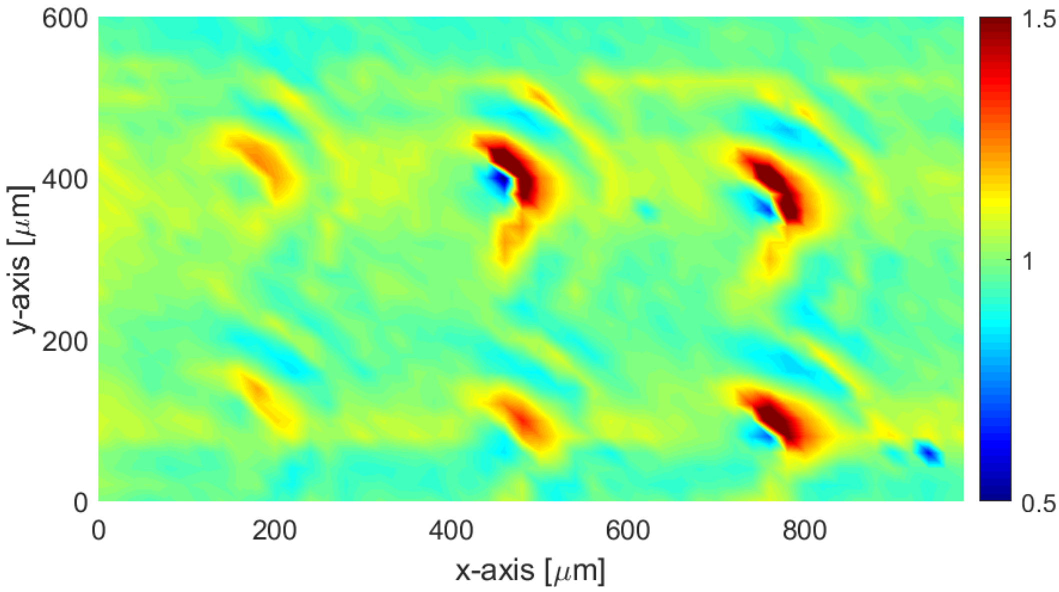

Figure 7: Measured scattered field around clustered defects (20 µm step size), incident wave top to bottom, A_0 mode at 5 MHz center frequency, amplitude from FFT, normalized, corrected for gradient; x = 200 µm: indent force 1 N; x = 500 µm: indent force 1.5 N; x = 800 µm: indent force 2 N.

In order to better understand the interaction of the high frequency guided wave with defects, the three wafers containing well separated defects with higher indent force (2 N, 3N and 4 N) were investigated. The amplitude of the scattered field was measured in a smaller area of 400 µm by 400 µm, but with higher resolution step size of 5 µm. This new measurement shows similar patterns in the vicinity of the indent, but with more details. To evaluate the correlation of this pattern with the indent size and force, several parameters were chosen for analysis (Fig. 8). The maximum normalized amplitude of the peaks and their orientation relative to the y-axis (angle δ) were computed. Where two peaks were visible in the scattered field, the peak spacing d was calculated. For smaller indents, where the two peaks merged to a single peak, the peak spacing was replaced by the FWHM (full width at half maximum). The interference length l and the normalized amplitude of the 1st fringe were extracted from the interference-like fringes in the upper right area of the scans.

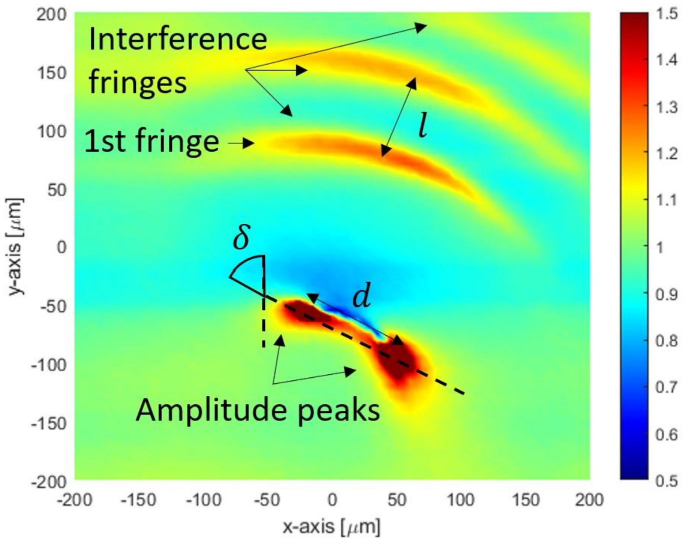

Figure 8: Typical pattern (FFT amplitude measurement, incident wave top to bottom) observed around individual indent at 5MHz with evaluation parameters marked; amplitude of peaks and angle δ with y-axis; peak separation distance d; interference length l between fringes and amplitude of first fringe.

Figure 9 presents the 6 FFT amplitude high-resolution scans for defects with a surface extent from approximately 50 µm to 100 µm (including the cracks). The exact localization of the defect center for the laser measurement proved difficult, and several steps as described in [27] were required to define the origin. Although a repeatable pattern was observed for the scattered wave field at the 6 defects, the guided wave amplitude after normalization shows some variability. The 6 measurements shown in Fig. 9 were evaluated to understand which of the parameters illustrated in Fig. 8 correlate with the defect size. Values are presented in Table 1.

High amplitude was observed at the center of each defect, as shown in Fig. 9. For the smaller defects (indent force 2 N: Fig. 9a, b), only a single peak was visible with a large amplitude variation between 1.1 and 4.8 of relative amplitude. For the larger defects (indent force 3 N: Fig. 9c, d, 4 N: Fig. 9e, f), two peaks with (normalized) amplitudes varying between 4.7 and 8.3 were observed. The peak separation d is similar to the defect surface extent, potentially showing that these quantities are correlated. However, it should be noted that the largest peak separation was actually observed for one of the 3N defects (Fig. 9c).

The values in Table 1 exhibit the variability visible in Fig. 9 for the peak measurement amplitude between indents of similar size (indent size increasing from left to right). The amplitudes of the main peak increase in general with the indent size, with the exception of measurement (c), which shows higher values for all parameters. The peaks of the amplitude maximum are extremely sharp with typically very high amplitude value (except for measurement (a)), even relative to the small scan step of 5 µm. Therefore, one can expect the peak amplitude to show high variability, since its value is based on a single measurement point. The peak orientation δ is similar for all indents ($\delta = 56 \pm 6$ °, mean and standard deviation) and correlates to the left-right asymmetry in the scattered amplitude pattern, which was also present in the measurement shown in Fig. 7. The origin of this asymmetry is not understood so far. Even though silicon has material anisotropy, for the geometry and orientation of the specimens and defects, symmetric scattered fields were expected. This might be correlated to effects of the laser measurement, as the laser spot size on the polished silicon wafer is quite large.

In front of the defects, the quarter-circular pattern of high and low amplitudes could be observed with more detail. The amplitudes of the 1st fringe increase in general with the indent size, again with the exception of measurement (c). It is important to stress that the fringes have different shapes compared to the main amplitude peaks, but a similar asymmetry relative to the incident wave direction can be seen. The interference fringes have smooth features, with limited amplitude variation over multiple measurement points, making the measurement of the amplitude evaluation quite robust. Similar to the amplitude of the main peak, significant variation of the fringe amplitude for the same indent force was observed. This is especially evident for the defects generated using the 3N indent force, where Fig. 9d shows a weak fringe pattern comparable to the 2N indents with only one fringe clearly visible, while the fringe pattern in Fig. 9c has the highest amplitude of all measured defects (see table 1).

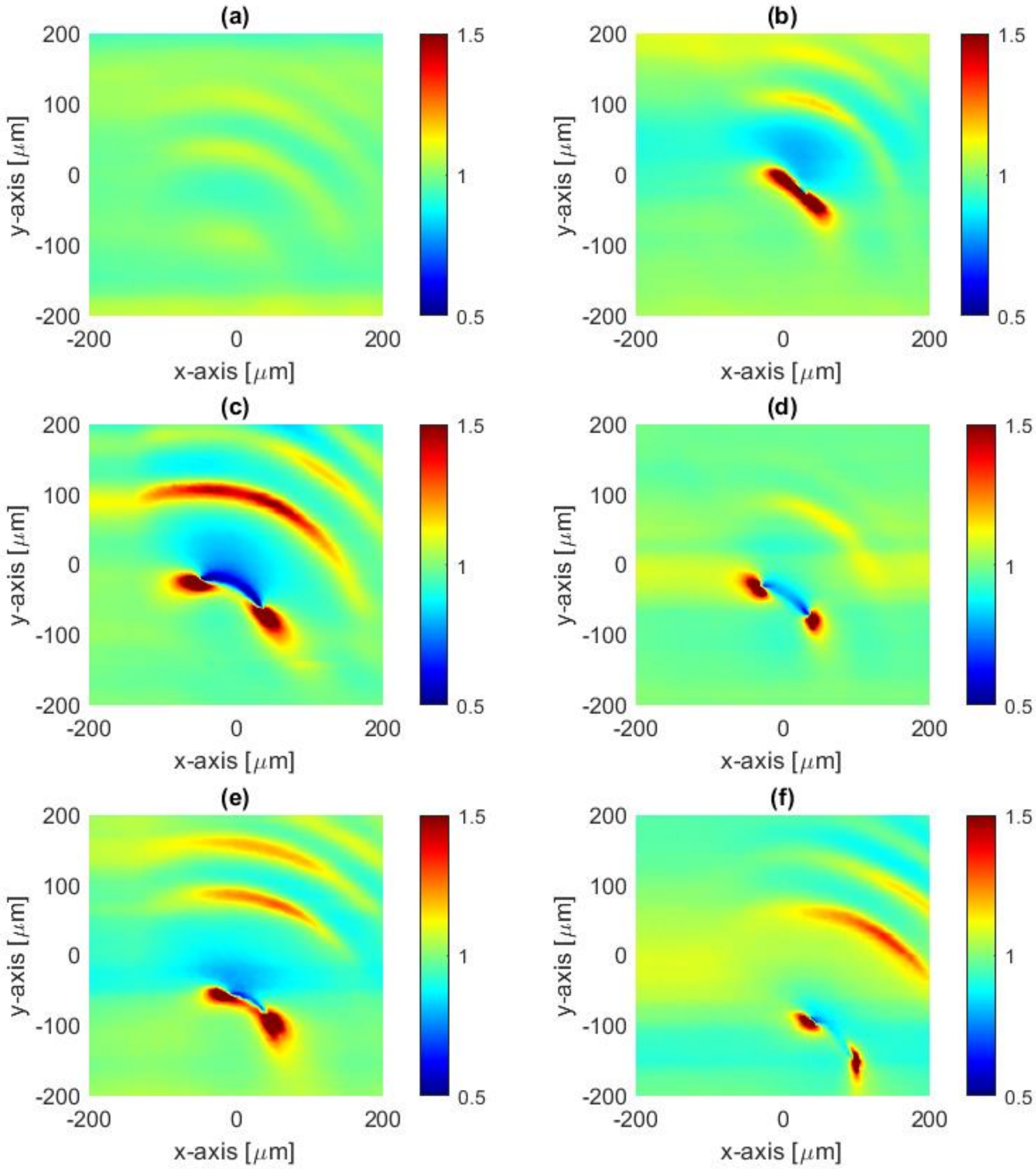

Figure 9: Measured scattered field around individual defects (5 µm step size), incident wave top to bottom, A_0 mode at 5 MHz center frequency, amplitude from FFT, normalized, corrected for gradient: (a), (b): 2N indent force; (c), (d) 3N indent force; (e), (f): 4N indent force.

Table 1: Characterization of the 6 measurements at individual defects shown in Fig. 9. Data with * shows FWHM for single amplitude peak; defect size average combined size of indent with cracks (horizontal and vertical).

	2N (a)	**2N (b)**	**3N (c)**	**3N (d)**	**4N (e)**	**4N (f)**
Defect size (μm)	52	54	76	80	94	95
Normalized peak amplitude	1.1*	4.8*	5.4	4.7	8.3	5.3
Peak orientation δ (°)	-	49*	64	59	59	49
Peak separation d (μm)	81*	71*	105	87	82	93
1st fringe amplitude	1.1	1.2	1.6	1.2	1.3	1.4
Interference length l (μm)	75	64	76	55	70	70

The distance between areas of high amplitudes (fringes) does not match the expected correlation to half of the wavelength of the A_0 wave mode for constructive and destructive interference of incident and scattered waves. The interference length l appears not to be correlated to the defect size and has similar values for all indents. The average interference length is $l = 68 \pm 7\ \mu m$ (mean and standard deviation) which is approximately 10 times smaller than the A_0 mode wavelength at 5 MHz (λ = 800 µm). As for the asymmetric wave field, parts of the observed pattern could be due to a combination or interference of the ultrasonic signal and optical artefacts from the laser system. Further investigations are required to clarify this hypothesis.

5. CONCLUSIONS

The applicability of high frequency guided ultrasonic waves for the detection of small surface defects in thin monocrystalline silicon wafers was investigated. In order to improve the efficiency and reduce the cost of renewable electricity generation using solar panels, reduction of wafer thickness and reliable detection of small surface cracking during the manufacture process are required. The propagation of guided waves in the anisotropic wafers was investigated, and good results were achieved experimentally for the A_0 Lamb wave mode at approximately 2 MHz mm frequency-thickness product with a strong beam and propagation range, allowing in principle inspection of complete wafers from a single excitation position.

A Vickers indenter with controlled force was used to create defects on the wafer surface. While penetrating into the brittle material, the indenter tip generated surface cracks propagating in the highest stiffness directions from each corner of the pyramid-like tip with a maximum surface extent of 100 µm. The scattering at these surface defects was measured using a non-contact laser interferometer. This showed a repeatable pattern consisting of sharp amplitude peaks at the center and fringes similar to the interference of incident and scattered waves, but with a smaller interference length than expected for the A_0 Lamb wave mode. A systematic asymmetry was clearly visible in the scattering patterns, which could not be explained from the silicon crystalline properties or the surface geometry of the defects. Parts of the observed pattern could be due to a combination or interference of the ultrasonic signal and optical artefacts from the laser system. Further investigations are required to clarify this hypothesis. The amplitude of the peaks and fringes in general increases with indent size and the main peak amplitude is significantly larger than the incident wave amplitude, making defect detection possible. It should be noted that the depth of the defects, except for the indent (up to 6 μm), is not known, and this might account for some of the observed variability.

Better characterisation of the depth profile of the generated micro-cracks and improved understanding of the scattered wave amplitude patterns will be required and could be obtained from numerical simulations or further measurements to better quantify the interaction and sensitivity of the proposed measurement methodology. Further investigation must also be done to characterize possible optical artefacts of the non-contact laser measurement for very small defects.

REFERENCES

[1] Luque, A. and Hegedus, S., Handbook of Photovoltaic Science and Engineering, Wiley, New York (2011).

[2] Papargyri, L., Theristis, M., Kubicek, B., Krametz, T., Mayr, C., and Papanastasiou, P., "Modelling and experimental investigations of microcracks in crystalline silicon photovoltaics: A review," Renewable Energy 145, 2387-2408 (2020).

[3] Abdelhamid, M., Singh, R., and Omar, M., "Review of microcrack detection techniques for silicon solar cells," IEEE J. Photovoltaics 4, 514-524 (2014).

[4] Israil, M., Ghani, A., and Kerm, Y., "Non-destructive microcracks detection techniques in silicon solar cell," Phys. Sci. Int. J. 4, 1073-1087 (2014).

[5] Belyaev, A., Polupan, O., Dallas, W., Ostapenko, S., Hess, D., and Wohlgemuth, J., "Crack detection and analyses using resonance ultrasonic vibrations in full-size crystalline silicon wafers," Appl. Phys. Lett. 88, 111907–111909 (2006).

[6] Rose, J.L., "Standing on the shoulders of giants: An example of guided wave inspection," Mat. Eval. 60, 53-59 (2002).

[7] Masserey, B. and Fromme, P., “Analysis of high frequency guided wave scattering at a fastener hole with a view to fatigue crack detection,” Ultrasonics 76, 78-86 (2017).

[8] Masserey, B. and Fromme, P., “In-situ monitoring of fatigue crack growth using high frequency guided waves,” NDT&E Int. 71, 1-7 (2015).

[9] Shen, Y., Wang, J., and Xu, W., “Nonlinear features of guided wave scattering from rivet hole nucleated fatigue cracks considering the rough contact surface condition,” Smart Mater. Struct. 27, 1-15 (2018).

[10] Poddar, B. and Giurgiutiu, V., "Complex modes expansion with vector projection using power flow to simulate Lamb waves scattering from horizontal cracks and disbonds," J. Acoust. Soc. Am. 140, 2123-2133 (2016).

[11] Leleux, A., Micheau, P., and Castaings, M., “Long range detection of defects in composite plates using Lamb waves generated and detected by ultrasonic phased array probes,” J. Nondestruct. Eval. 32, 200-214 (2013).

[12] Chapuis, B., Terrien, N., and Royer, D. “Excitation and focusing of Lamb waves in a multilayered anisotropic plate,” J. Acoust. Soc. Am. 127, 198-203 (2010).

[13] Murat, B.I.S., Khalili, P., and Fromme, P., “Scattering of guided waves at delaminations in composite plates,” J. Acoust. Soc. Am. 139, 3044-3052 (2016).

[14] Potel, C., Baly, S., de Belleval, J.-F., Lowe, M., and Gatignol, P., “Deviation of a monochromatic Lamb wave beam in anisotropic multilayered media: asymptotic analysis, numerical and experimental results,” IEEE Trans. Ultrason. Ferroel. Freq. Contr. 52, 987-1001 (2005).

[15] Veidt, M. and Sachse, W., “Ultrasonic point-source/point-receiver measurements in thin specimens,” J. Acoust. Soc. Am. 96, 2318-2326 (1994).

[16] Maris, H.J., “Enhancement of heat pulses in crystals due to elastic anisotropy,” J. Acoust. Soc. Am. 50, 812-818 (1971).

[17] Kim, K.Y., Bretz, K.C., Every, A.G., and Sachse, W. "Ultrasonic imaging of the group velocity surface about the cubic axis in silicon," J. Appl. Phys. 79, 1857-1863 (1996).

[18] Audoin, B., Bescond, C., and Deschamps, M., "Measurement of stiffness coefficients of anisotropic materials from pointlike generation and detection of acoustic waves," J. Appl. Phys. 80, 3760-3771 (1996).

[19] Prada, C., Clorennec, D., Murray, T.W., and Royer, D., "Influence of the anisotropy on zero-group velocity Lamb modes," J. Acoust. Soc. Am. 126, 620-625 (2009).

[20] Youngjae, M., Gyeongwon, Y., Kyung-Min, K., Yuji, R., and Young, K., "Comparison of slowness profiles of Lamb waves with elastic moduli and crystal structure in single crystalline silicon wafers," J. Korean Soc. Nondestruct. Test. 36, 2016.

[21] Fromme, P., Pizzolato, M., Robyr, J.-L., and Masserey, B., "Lamb wave propagation in monocrystalline silicon wafers," J. Acoust. Soc. Am. 143, 287-295 (2018).

[22] Pizzolato, M., Masserey, B., Robyr, J.-L., and Fromme, P., "Guided ultrasonic wave beam skew in silicon wafers," AIP Conf. Proc. 1949, 090005 (2018).

[23] Song, M.-K. and Jhang, K.-Y., "Crack detection in single-crystalline silicon wafer using laser generated Lamb wave," Adv. Mater. Sci. Eng. 2013, 950791 (2013).

[24] Chakrapani, S.K., Padiyar, M.J., and Balasubramaniam, K., "Crack detection in full size Cz-silicon wafers using lamb wave air coupled ultrasonic testing (LAC-UT)," J. Nondestruct. Eval. 31, 46–55 (2012).

[25] Li, Y., He, C., Lyu, Y., Song, G., and Wu, B., "Crack detection in monocrystalline silicon solar cells using air-coupled ultrasonic Lamb waves," NDT&E Int. 102, 129-136 (2019).

[26] Simon, M., Masserey, B., Robyr, J.-L., and Fromme, P., "High frequency guided wave defect imaging in monocrystalline silicon wafers," Proc. SPIE 10972, 1097206 (2019).

[27] Lauper, M., Fromme, P., Robyr, J.-L., and Masserey, B., "Silicon wafer defect detection using high frequency guided waves," Proc. SPIE 10600, 106000G (2018).

[28] Masserey, B., Simon, M., Robyr, J.-L., and Fromme, P., "Defect detection in monocrystalline silicon wafers using high frequency guided waves," AIP Conf. Proc. 2102, 020013 (2019).

[29] Pavlakovic, B., Lowe, M. J. S., Alleyne, D., and Cawley, P., "Disperse: A general purpose program for creating dispersion curves," Proc. QNDE 16, ed. by D.O. Thompson and D. Chimenti, Plenum, New York, 185-192 (1997).